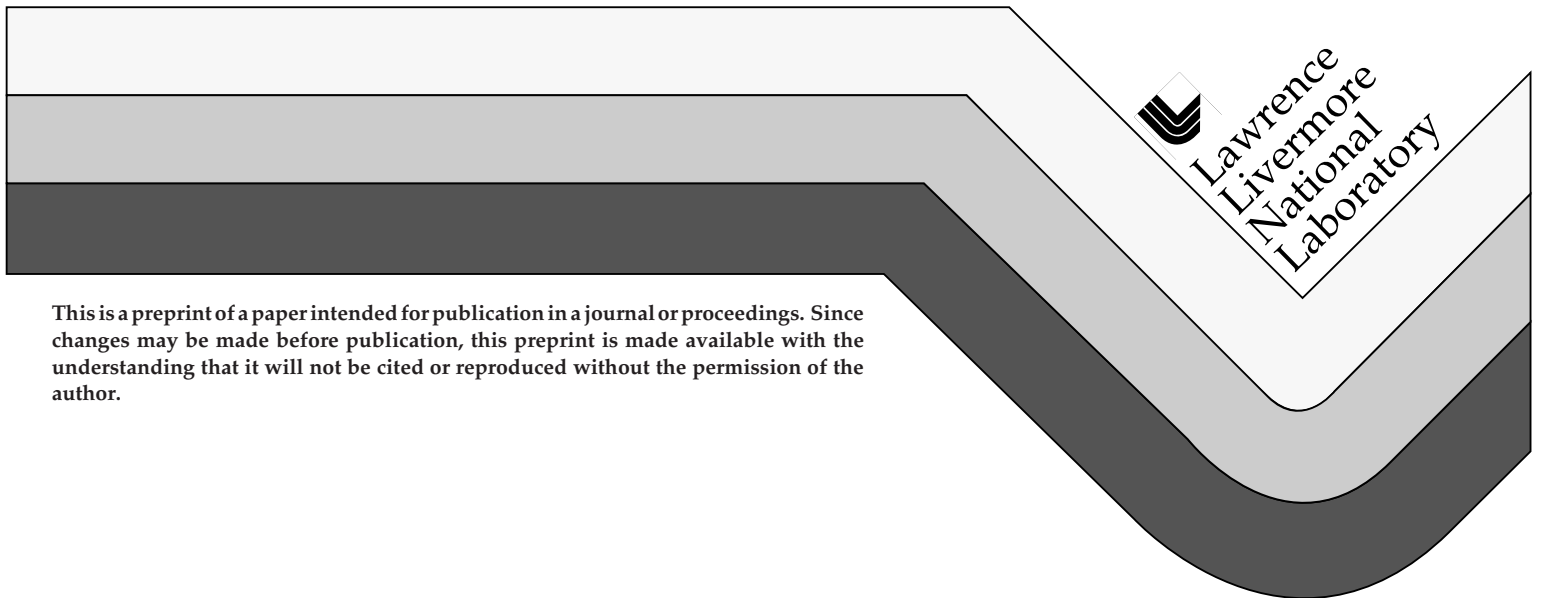


## Cryogenic Detector Development at LLNL: Ultraviolet, X-ray, Gamma-ray and Biomolecule Spectroscopy

S. E. Labov, M. Frank, J. B. le Grand, M. A. Lindeman, H. Netel, L. J. Hiller,  
D. Chow, S. Friedrich, C. A. Mears, G. Caldara, A. T. Barfknecht

This paper was prepared for submittal to the  
Seventh International Workshop on Low Temperature Detectors  
Munich, Germany  
July 27-August 2, 1997

August 12, 1997



This is a preprint of a paper intended for publication in a journal or proceedings. Since changes may be made before publication, this preprint is made available with the understanding that it will not be cited or reproduced without the permission of the author.

#### DISCLAIMER

This document was prepared as an account of work sponsored by an agency of the United States Government. Neither the United States Government nor the University of California nor any of their employees, makes any warranty, express or implied, or assumes any legal liability or responsibility for the accuracy, completeness, or usefulness of any information, apparatus, product, or process disclosed, or represents that its use would not infringe privately owned rights. Reference herein to any specific commercial product, process, or service by trade name, trademark, manufacturer, or otherwise, does not necessarily constitute or imply its endorsement, recommendation, or favoring by the United States Government or the University of California. The views and opinions of authors expressed herein do not necessarily state or reflect those of the United States Government or the University of California, and shall not be used for advertising or product endorsement purposes.

# Cryogenic detector development at LLNL: ultraviolet, X-ray, gamma-ray and biomolecule spectroscopy

Simon E. Labov<sup>1</sup>, M. Frank<sup>1</sup>, J.B. le Grand<sup>1</sup>, M.A. Lindeman<sup>1</sup>, H. Netel<sup>1</sup>, L.J. Hiller<sup>1</sup>, D. Chow<sup>1</sup>, S. Friedrich<sup>1</sup>, C.A. Mears<sup>1</sup>, G. Caldara<sup>1</sup>, A.T. Barfknecht<sup>2</sup>

<sup>1</sup>*Lawrence Livermore National Laboratory, P.O. Box 808, L-401, Livermore CA 94550, USA*

<sup>2</sup>*Conductus, Inc., 969 West Maude Ave., Sunnyvale, CA 94086, USA*

## Abstract

We are developing low-temperature detectors for optical, ultraviolet, X-ray, and gamma-ray spectroscopy, and for biomolecular mass spectrometry. We present here a survey of our recent work in developing these detectors and some of the first results in applying these detectors for materials analysis and biomolecular mass spectrometry. We have measured thin-film Nb/Al/Al<sub>2</sub>O<sub>3</sub>/Al/Nb superconducting tunnel junction (STJ) X-ray detectors in the 0.2 to 1 keV band with a range of different junction sizes and aluminum film thicknesses. In one case, we have achieved the statistical limit to the energy resolution in this band. We have measured the performance of these STJ detectors as a function of count rate and demonstrated a resolution of 13 eV FWHM at 277 eV with an output count rate of 20,600 cts/s. Using X rays from a synchrotron light source to study composite materials, we have demonstrated that we can resolve the L lines of transition metals from the nearby K lines of light elements. We describe the first use of a low-temperature X-ray detector to measure X-ray fluorescence from the dilute metal component in a protein. In a time-of-flight mass spectrometry experiment using Nb/Al<sub>2</sub>O<sub>3</sub>/Nb STJ detectors operating at 1.3 K, we have demonstrated that masses as large as 750 kDa can be detected in a time-of-flight mass spectrometer. This extends the mass range for this type of mass spectrometer by an order of magnitude. We also show that the energy resolving capability of the STJ can be used to measure the charge of the molecule, thus removing ambiguities in the measured mass spectrum. We describe the development of X-ray and gamma-ray spectrometers using small crystals of Ta with STJ and superconducting transition-edge sensors (TES). We present a new model for TES microcalorimeter that includes both the temperature and current dependence of the TES.

## 1 STJ detectors

We have developed a Nb/Al/Al<sub>2</sub>O<sub>3</sub>/Al/Nb STJ production process at Conductus Inc. that allows us to fabricate detectors with very thin and very uniform Al<sub>2</sub>O<sub>3</sub> tunnel

barriers [1]. Using these devices and a dc SQUID-array current amplifier, we measured a resolution of 29 eV FWHM at 6 keV [2, 3]. The SQUID amplifier also allowed us to obtain a resolution of 21 eV FWHM at 2.6 keV with a detector 282 × 282 μm<sup>2</sup> [4]. Measurements between 1 and 8 keV show a very linear response [5]. These detectors, however, perform best at X-ray energies below 1 keV. At these energies the detectors are nearly 100% efficient, and we previously obtained a resolution of 12.5 eV FWHM at 1 keV [6]. This device was measured with a standard FET-based current amplifier, and used a thin 50 nm aluminum "trapping" layer which allowed operation at temperatures up to 600 mK.

In Fig. 1 we show a schematic cross section of our STJ detectors. The detectors consist of a 265 nm thick Nb base layer and a 165 nm thick Nb counter electrode separated by a thin (~20 Å) Al<sub>2</sub>O<sub>3</sub> tunnel barrier with Al "trapping" layers on each side of the barrier. The thickness of the Al trapping layers range from 35 to 200 nm. The detectors are diamond-shaped with sizes ranging from 20 × 20 μm<sup>2</sup> to 200 × 200 μm<sup>2</sup>. These detectors were fabricated at Conductus, Inc., using a modified photolithographic Nb trilayer process [1]. The SiO<sub>2</sub> layer covering the devices was removed to allow low-energy X-rays to reach the detector. During operation a small magnetic field ( $B \sim 10$  mT) is applied parallel to the tunnel barrier in order to suppress the dc Josephson current in the device. This suppression is necessary to allow stable operation of the device when biased near zero voltage.

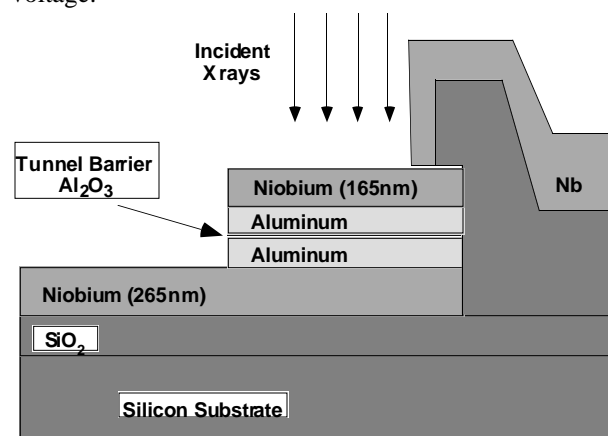


Fig. 1 Cross section of STJ X-ray detector

During operation the detector is cooled to well below the critical temperature of the superconducting layers such that nearly all conduction electrons are bound into Cooper pairs and the number of thermal excitations is small. For the 50 nm-thick Al trap devices, this is the case below  $\sim 500$  mK. The detectors with 200 nm-thick Al traps operate best below 300 mK. The absorption of an X-ray photon in one of the superconducting electrodes breaks Cooper pairs creating quasiparticles, which can quantum-mechanically tunnel through the  $\text{Al}_2\text{O}_3$  barrier. When a small bias voltage is applied across this tunnel barrier the tunneling of the quasiparticles creates a measurable current signal. The amplitude of the current pulse is proportional to the number of quasiparticles produced and thus to the energy of the absorbed X-ray photon.

We refer to the Al layers as quasiparticle traps. The process of "quasiparticle trapping" [7] relies on the fact that the Al layers have a lower superconducting energy gap than the Nb layers. Therefore, when the quasiparticles diffuse to one of the Al layers they can relax energetically by emitting a phonon. With a correspondingly lower energy they cannot return into the Nb and thus become trapped in the Al. This concentrates quasiparticles near the tunnel barrier increasing the tunnel rate and hence the signal. The traps also reduces quasiparticles losses because the quasiparticle loss rate tends to be higher in Nb than in Al.

A schematic of the experimental setup used for the measurements discussed here is shown in Fig. 2. The STJ detector was housed in a pumped liquid helium cryostat equipped with an adiabatic demagnetization refrigerator (ADR) unit with a base temperature of  $\sim 50$  mK [8, 9]. During the experiments the temperature was *not* regulated and allowed to drift up freely.

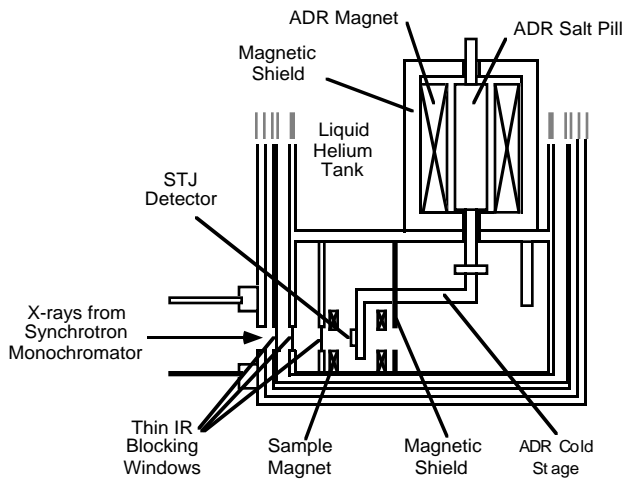


Fig. 2 Schematic of the experimental setup.

The X-ray experiments presented here were performed at the Stanford Synchrotron Radiation Laboratory (SSRL). The cryostat was mounted onto an xyz stage and connected to the synchrotron beam line with a flexible bel-

lows. By moving the cryostat we could align the detector with the synchrotron beam. Moving the detector in and out of the center of the beam provided a convenient way of adjusting the count rate. Three thin windows were placed into the 77 K shield, the 2 K shield and the magnetic shield (also at 2 K) in front of the detectors to limit the exposure of the detectors to infrared radiation emitted from the beam line at 300 K. These windows consisted of 200 Å aluminum and 1000 Å of parylene on an 80 % open Ni mesh.

We used an FET-based preamplifier with fast ( $\sim 0.25$  to  $1.0$   $\mu\text{s}$ ) negative feedback to measure the current signal from the STJ detector. The rise time of the current pulses was limited by this amplifier to typically  $\sim 0.5$   $\mu\text{s}$ , the decay time of the current pulses was given by the quasiparticle life time. During most measurements we also injected pulses with similar shape from a pulse generator into the electronics to monitor the electronic noise. The X-ray induced current pulses and pulses from the pulse generator were further amplified and shaped either with an Ithaco 4302 filter amplifier with adjustable band pass or with a Canberra 2020 spectroscopy amplifier with a baseline restorer. The shaped pulses were then fed into a pulse height analyzer without any further signal processing. No pile-up rejection was used.

## 2 Theoretical Resolution Achieved with Soft X rays

As described below, we measured a series of 16 different detectors with four different sizes and four different Al trapping layer thickness. Of the 16 detectors measured for this study, the best overall resolution was obtained with the  $50 \times 50$   $\mu\text{m}^2$  detector with 200 nm-thick Al trapping layers. The spectra are very clean and free of artifacts, and the detector response is almost linear. An example of a spectrum is shown in Fig. 3.

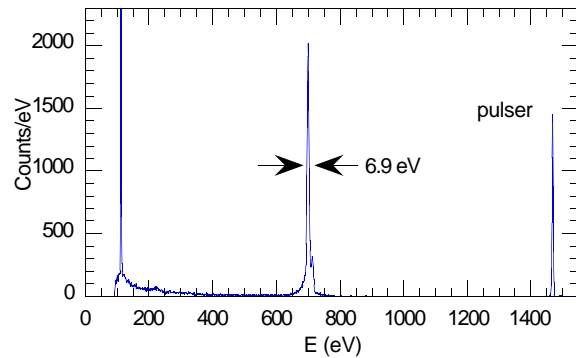


Fig. 3. X-ray spectrum at 700 eV obtained with  $50 \times 50$   $\mu\text{m}^2$  STJ detector with 200 nm-thick Al trapping layers.

This spectrum shows three very narrow peaks. The middle peak shows the response to 700 eV X rays, the other two peaks are due to the test pulser. Below the X-ray peak, some counts are seen which are due to white light scattered from the grating of the monochromator. In spectra up to 650 eV the shape of the X-ray peaks are very Gaussian. For X-ray energies of 700-1000 eV, the central part of the lines are very Gaussian, but additional wings were present on both the low and the high energy sides of the lines.

In Fig. 4 we show the resolution of this detector as a function of energy. The solid squares in Fig. 4 indicate the line widths obtained by measuring the width of the actual line at half the observed maximum height. Neither fitting, nor continuum or tail subtractions were used. The resolution ranges from 4.4 eV FWHM at 200 eV to 11.6 eV FWHM at 1 keV. Some of the measured width at energies above 700 eV is due to the energy width of the monochromator. This contribution is indicated by the dotted line in Fig. 4.

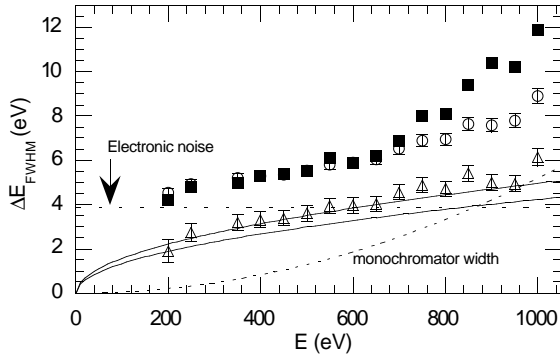


Fig 4. Resolution of  $50 \times 50 \mu\text{m}^2$  STJ detector with 200 nm-thick Al trapping layers. Squares show full width, open circles show width from a fit, open triangles show the intrinsic resolution. Upper and lower solid lines show the theoretical resolution with and without quasiparticle multiplication respectively.

To understand why the peaks have the observed shape and width, we fit the peaks to a Gaussian profile. At energies below 600 eV, the Gaussian profile usually fits quite well, and the line widths from fitting agree with the line widths determined by directly measuring the FWHM. At higher energies the additional structure in the wings must be taken into account. This structure is typically asymmetric. Below the peak there is a tail, while above the peak there is more often an extra small peak or bump. The mechanisms which contribute to these features include X rays which are absorbed in the base electrode and Al layers [10], self-recombination [11], variations in the depth at which the X rays are absorbed, and residual  $\text{SiO}_2$  or other surface contaminants.

To fit the central peak to a Gaussian profile we first subtract off any white light which scatters through the monochromator, and then we subtract off any non-Gaussian wing structure. A Gaussian profile then fits quite well to the central peak. We find that by varying how the wing structure is subtracted gives a variation in the width of about 4%. The widths derived from fitting just the central part of the peak are indicated by circles in Fig. 4.

Now to determine the intrinsic resolution of the counter electrode, we subtract in quadrature the electronic noise and the intrinsic energy width of the X-ray beam. The electronic noise for this detector was 3.9 eV FWHM, and is shown by the dashed line in Fig. 4. For the monochromator slit settings used, the energy width of the X-ray beam increases quadratically with energy reaching 5.2 eV at 1000 eV, as shown by the dotted line in Fig. 4. The intrinsic resolution, indicated by triangles in Fig. 4, varies with the square root of the energy. Fitting the width as a function of energy we find

$$\Delta E_{FWHM} = (0.170 \pm 0.014)\sqrt{E} \quad (1)$$

with  $\Delta E$  and  $E$  in eV.

The theoretical resolution of a symmetric junction without quasiparticle multiplication is:

$$\Delta E_{FWHM} = 2.35\sqrt{\varepsilon(F + F')E} \quad (2)$$

where  $\varepsilon$  is the average energy required to produce one quasiparticle,  $F$  is the Fano factor describing the statistical distribution in the number of quasiparticles created. The  $F'$  term, which was originally described by Mears *et al.* [12] and later expanded by Goldie *et al.* [13], accounts for the additional statistical fluctuations due to multiple tunneling of the quasiparticles back and forth through the tunnel barrier. For Nb we assume  $F = 0.2$  and  $\varepsilon = 1.7 \Delta_{\text{Nb}}$  [14, 15]. For symmetric junctions  $F' = 1 + 1/n$  where  $n$  is the average number of times each quasiparticle tunnels through the barrier. For this detector  $n \approx 13$  so the theoretical resolution without quasiparticle multiplication is:

$$\Delta E_{FWHM} = 0.134\sqrt{E} \quad (3)$$

which is plotted as a solid line in Fig. 4.

The measured result in Eq. 1 is very close to the calculated resolution in Eq. 3. Moreover the remaining small difference can be explained by the fact that for the detectors with 200 nm of Al, the measured gap in the Al  $\Delta_{\text{Al}} = 0.34$  meV is less than a third of the Nb gap  $\Delta_{\text{Nb}} = 1.5$  meV. When a quasiparticle is trapped from the Nb into the Al, a phonon as large as 1.16 meV may be produced, which is energetic enough to break up another Cooper pair in the Al producing two more quasiparticles. Since not every quasiparticle that gets trapped will multiply, statistical fluctuations in the number of quasiparticles produced during this multiplication will further broaden the resolution [16]. We find this multiplication can increase the expected resolution up to:

$$\Delta E_{FWHM} = 0.157\sqrt{E}. \quad (4)$$

This is shown by the solid line in Fig. 4 which is within the error of the measured resolution. We therefore conclude that the intrinsic resolution we measured for this detector is well described by the theory including the statistical fluctuations in the number of quasiparticles that are created, the fluctuations in the number of quasiparticles produced in multiplication and the fluctuations in the number of quasiparticles tunneling through the barrier.

### 3 Resolution at High Count Rates

One of the advantages of superconductor insulator superconductor STJ X-ray detectors is their fast response. The length of the current pulse we observe is determined by the quasiparticle lifetime in the device. For the junctions with 50 nm-thick Al trapping layers, this was about 4.5  $\mu$ s. This fast response allows operation at much higher count rates than thermal microcalorimeters [17-20].

To explore the count rate capability of these detectors, we measured a detector  $141 \times 141 \mu\text{m}^2$  with 50 nm thick Al trapping layers. We irradiated this detector with 277 eV X rays which corresponds to the energy of carbon K. The count rate was adjusted to the desired values by adjusting the cryostat position and moving the detector closer to the center of the synchrotron beam. The Canberra 2020 spectroscopy amplifier was used including its automatic baseline restorer. For count rates up to 10,000 cts/s optimal results were achieved with shaping times of 3-4  $\mu$ s, above 10,000 cts/s with 1.5  $\mu$ s. No pile-up rejection was applied.

At the low count rate of 375 cts/s the resolution was  $5.9 \pm 0.1$  eV (FWHM), as shown in Fig. 5. The electronic noise in this measurement was  $4.5 \pm 0.1$  eV (FWHM).

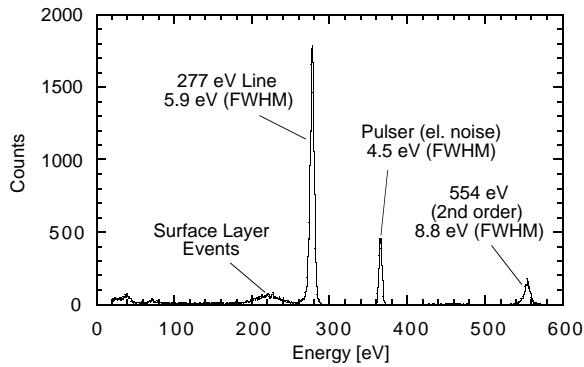


Fig 5. X-ray spectrum at 277 eV obtained with  $141 \times 141 \mu\text{m}^2$  STJ detector with 50 nm-thick Al trapping layers. Count rate was 375 cts/s

In Fig. 6 we show an X ray spectrum measured at a count rate of 23,300 cts/s. The count rate quoted here was the output count rate of the pulse height analyzer as determined from the total number of counts in the spectrum

and the active time of the pulse height analyzer excluding the dead time, which was 13 % in this measurement. The 277 eV line is resolved with a FWHM energy resolution of  $13.0 \text{ eV} \pm 0.1 \text{ eV}$ . The energy calibration was performed using the second-order X-ray line at 554 eV resolved with  $15.7 \pm 0.2 \text{ eV}$  (FWHM). The resolution was largely dominated by the electronic noise of  $11.9 \pm 0.1 \text{ eV}$  as measured from the width of the pulser line. The increase of this electronic noise compared to the electronic noise measured at low count rate was caused by baseline fluctuations resulting from the large count rate, pulse pile-up and imperfect baseline restoration. The contribution of the intrinsic energy width of the beam was negligible.

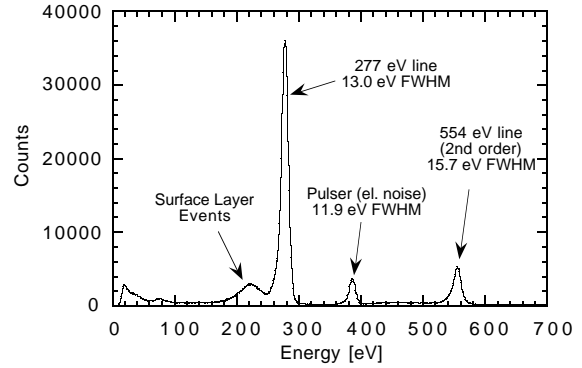


Fig 6. Same as Fig 5. but with count rate of 23,300 cts/s

In Fig. 7 the measured FWHM energy resolution at 277 eV incident X-ray energy (filled circles) and 554 eV (2nd order X-rays, filled squares) is plotted together with the measured electronic noise (open circles) as function of the count rate. Increasing the count rate from low rates of several 100 Hz, the resolution at 277 eV remained nearly constant at 6-8 eV FWHM up to a several 1000 cts/s.

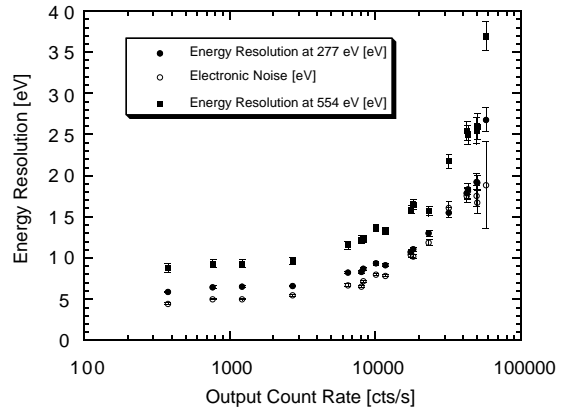


Fig. 7. Total FWHM energy resolution at 277 eV.

The resolution at 277 eV remained below 10 eV for count rates up to  $\sim 10,000$  cts/s and then degraded to 13 eV at 23,000 cts/s and 20 eV at 50,000 cts/s. At 50,000 cts/s the PHA dead time approached 30 %. Above 50,000 cts/s the resolution seemed to degrade rapidly, presumably due to significant pulse pile up. These results could probably be improved further by applying additional signal processing techniques such as pile-up rejection. The high count rate measurements are discussed in more detail in Frank *et al.* [21].

## 4 STJ Performance as a Function of Al Thickness and Junction size

To better understand the behavior of these devices, we fabricated a series of detectors with similar tunnel barrier characteristics but with different aluminum "trapping" layer thicknesses. Previous measurements of this type have been performed with 6 keV X rays and similar detectors [22], and with detectors that have thinner Al layers [23]. Here we describe measurements of detector response to soft X-rays from 0.2 to 1 keV, using detectors with both a range of aluminum trapping layer thickness, and a range of junction sizes.

We measured detectors with four different Al trapping layer thicknesses: 35 nm, 50 nm, 100 nm and 200 nm. For each Al trap thickness, we measured detectors of four different sizes:  $20 \times 20 \mu\text{m}^2$ ,  $50 \times 50 \mu\text{m}^2$ ,  $70 \times 70 \mu\text{m}^2$  and  $141 \times 141 \mu\text{m}^2$  making up for a total of 16 junctions. We illuminated each of these detectors with X rays ranging from 200 eV to 1000 eV in 50 eV steps. For all measurements similar conditions were used as much as possible. The X-ray pulses were filtered using the Ithaco 4302 with a 1 MHz low pass filter and a 3.15 kHz high pass filter. These settings appear to work reasonably well for all junctions even though the pulse length varied from 1.2 to 9  $\mu\text{s}$ . We did not optimize the filter settings for each detector. Instead, we chose a relatively large band pass of 3.15 kHz to 1 MHz for the pulse shaping in order to not distort the pulse shape too much. While this way of pulse shaping is not optimal for achieving best energy resolution it allows us to compare the pulses from different STJs with decay times ranging from 1.2 to 9  $\mu\text{s}$ .

The bias voltage was roughly optimized for each junction, ranging from 0.2-0.3 mV for the junctions with 200 nm Al traps, up to about 0.5 mV for the devices with 35 nm Al traps. The bias current varied strongly from junction to junction and not always proportional to the junction area, indicating either some residual trapped flux or variations in the quality of the junctions. For these measurements the current amplifier had a feed back time of 1  $\mu\text{s}$  and the detector count rate was limited to 200 cts/s where the effect of count rate on energy resolution was negligible.

Each peak arising from X rays absorbed in the counter electrode was fit to a Gaussian. When necessary to achieve a reasonable fit, the extra wing structures were subtracted before fitting a Gaussian to the central part of the line. To find the line width intrinsic to each detector, the electronic noise and any contribution from the monochromator were subtracted in quadrature from the measured width.

All junctions showed a fairly linear response. The pulse height as a function of energy is well described by a second order polynomial with only a small quadratic correction:

$$I_{ch} = A_0 + A_1 E + A_2 E^2 \quad (5)$$

where  $I_{ch}$  is the current pulse height in channels and  $E$  is the X-ray energy. The offset  $A_0$ , comes from the analog to digital converter and is of no consequence. As the nonlinearity is only a few percent, the detector response is mainly characterized by  $A_1$ . The  $A_2$  term indicates the degree of nonlinearity in the detector.

The width of the peaks were then analyzed as a function of energy. For each junction we fit the width to a linear function of the energy and to a square root function of the energy. We examined  $\chi^2_v$  for each fit to determine which type of dependence better characterized each detector. If the resolution of a junction is proportional to the energy, then we infer that response varies with the location of the X-ray absorption. If the resolution is proportional to the square root of the energy, then we infer a statistical process is involved.

The response term  $A_1$  is shown as a function of Al trap thickness in Fig. 8.

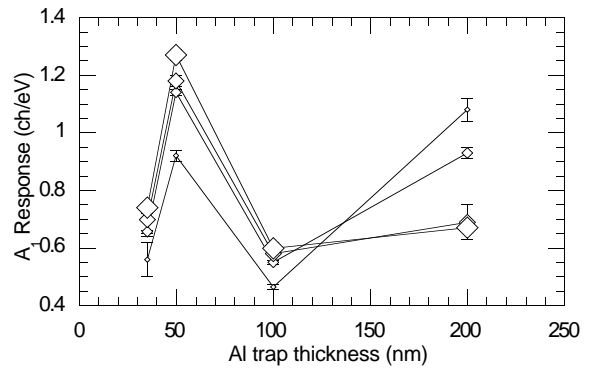


Fig 8. The STJ response  $A_1$  as a function of Al trap thickness. The size of the symbols relates to the size of the junctions.

The highest response is from the detectors with Al trapping layers 50 nm thick. For the detectors with 35 nm-thick Al layers, the response is considerably smaller. This is most likely due to the large energy gap in the thin Al layer and the slower trapping that results. The junctions with 100 nm-thick Al traps show less signal than the devices with Al 50 nm thick. This is due to the

lower tunneling rate. The junctions with Al traps 200 nm thick show again a larger signal. This is most probably caused by quasiparticle multiplication, as discussed in Section 2 above.

In Fig. 9 we plot the  $A_1$  response term as a function of junction size. There is a tendency of increasing signals with increasing size. This is true except for the junctions with Al trapping layers 200 nm thick. The effect is strongest for the  $20 \times 20 \mu\text{m}^2$  junctions. For this size the self recombination of quasiparticles may be strong. This is supported by the fact that these devices are also strongly nonlinear (see below). Also the proximity of edges and leads may provoke a decrease of the signal with decreasing size. We do not yet understand the strong deviation in the behavior observed for the junctions with 200 nm thick Al trapping layers. This may be due to magnetic flux trapped in the devices, although great care was taken to avoid trapped flux.

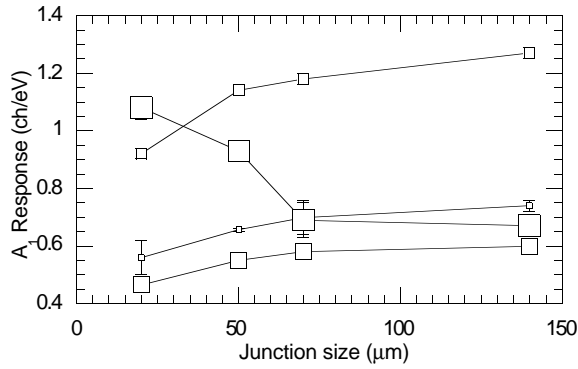


Fig. 9. The STJ response  $A_1$  as a function of junction size. The size of the symbols relates to the thickness of the Al trapping layers.

The nonlinearity coefficient  $A_2$  is shown as a function of junction size in Fig. 10.

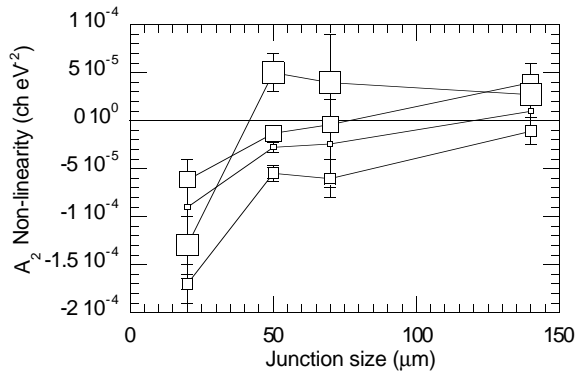


Fig. 10. The nonlinearity coefficient  $A_2$  as a function of junction size. The size of the symbols relates to the thickness of the Al trapping layers.

As evident in Fig. 10, the response of the  $20 \times 20 \mu\text{m}^2$  junctions is significantly nonlinear. This is due to self-recombination. For most of the  $50 \times 50 \mu\text{m}^2$  junctions the signal is still slightly nonlinear. For the larger junctions the response is linear, with  $A_2$  close to zero.

For most of the detectors the intrinsic resolution was best fit to a linear function of energy. For some of the better junctions with 50 or 200 nm-thick Al layers, the square root dependence is a much better fit. In Fig. 11 we show the intrinsic resolution of each detector at 1 keV. The resolution of the  $20 \times 20 \mu\text{m}^2$  detectors is particularly bad because of the proximity of the lead and the edges. The junctions with 35 nm-thick Al trapping layers also show poor resolution. This is probably because the thin trapping layers are not very efficient at trapping quasiparticles, which means the quasiparticles will spend more time in the Nb layers where we expect a higher quasiparticle loss rate. The resolution of the junctions with 100 nm-thick Al traps is slightly worse than the junctions with 50 and 200 nm-thick Al traps. This is probably because of the small signals these junctions produce. A more detailed discussion of these measurements is in preparation [24].

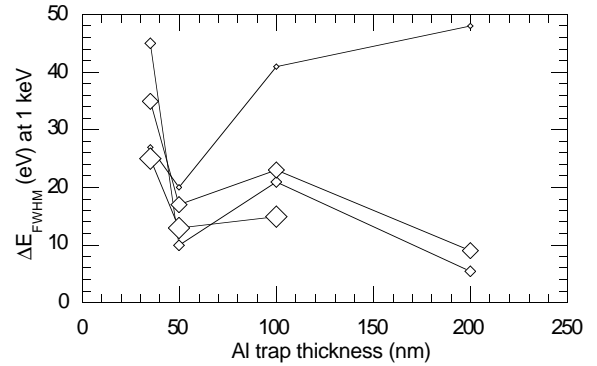


Fig. 11. The intrinsic resolution of the STJ detectors as a function of Al trap thickness. The size of the symbols relates to the size of the junctions.

## 5 X-ray fluorescence

The performance of our STJ detectors below 1 keV is very good, with energy resolution often below 10 eV, about ten times better than can be achieved with semiconductor ionization detectors. Also, below 1 keV the niobium counter electrode absorbs most of the incident X-ray photons. To start taking advantage of the performance of these detectors, we have begun to use them in experiments requiring X-ray fluorescence analysis with high spectral resolution for soft X rays. For most of these experiments, we used a  $141 \times 141 \mu\text{m}^2$  detector with 50 nm-thick Al traps.



In Fig. 12 we show the X-ray fluorescence spectrum obtained with a sample consisting of boron nitride covered partially with titanium powder excited by 500 eV X rays. This sample was chosen to simulate B and TiN, which are important materials in semiconductor fabrication. The K lines of B, N and the L line of Ti are well separated in this spectrum. Also present in this spectrum are K lines from C and O, presumably from oxides and contamination in the sample, and an X-ray line at 500 eV from scattered incident X rays. The FWHM energy resolution of the X-ray lines ranges from 9.6 eV for C K to 13.1 eV for Ti L. The electronic noise in this measurement was 6.7 eV as indicated by the width of the pulser line. For comparison, the resolution of Si(Li) detectors in this energy range is about a factor 10 worse and not sufficient to separate the Ti L line from N K.

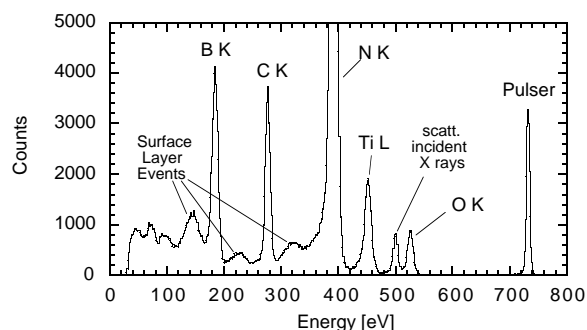


Fig. 12. Fluorescence spectrum obtained with a BN sample coated with Ti powder.

The K lines of B, C and N in Fig. 12 are each accompanied by a "hump" of events at the low-energy side of the line labeled "surface layer events." These humps probably originate from events caused by X-rays absorbed in a less responsive surface layer of our detector. Such a surface layer may be composed of niobium oxide, residues of SiO<sub>2</sub> from the detector fabrication process or other surface contamination. These surface layers predominantly affects the lower energy X rays. We have found that detectors from some wafers do not show these artifacts. The exact origin of these surface layer events and the other background seen at the low-energy end of the spectrum is still under study.

In Fig. 13 we show part of a fluorescence spectrum measured with a sample from a magnetic storage disk fabricated by IBM with 1000 eV incident X rays. The composition and thickness of the various metal layers in this sample is indicated on the right side of this figure. Most of the L lines of the transition elements present in the sample (Cr, Co and Ni) are resolved from each other and indications for some substructures of the lines are visible. The resolution in the energy range shown was 10–15 eV. With these L lines resolved one can, in principle, determine the composition and thickness of the various layers

in the sample using the measured fluorescence intensities for the various elements and the fundamental parameter method [25].

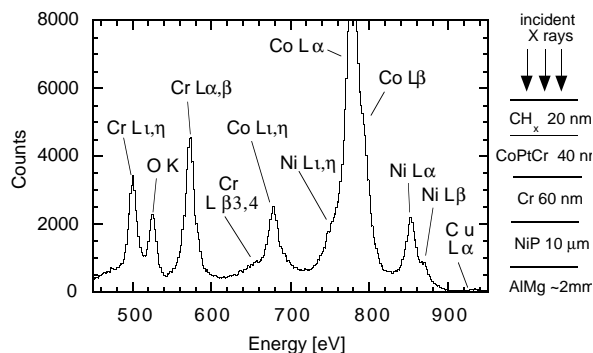


Fig. 13. Fluorescence spectrum from a magnetic storage disk with 1 keV incident X-rays.

In Fig. 14 we show part of a fluorescence spectrum measured with a manganese oxide sample and an incident beam energy of 700 eV. The Mn L lines are well resolved from the large O K line. The F K and Fe L lines are probably due to contamination of the sample. The energy resolution of the O K line is 9.6 eV FWHM and the electronic noise was 4.6 eV. With the measured resolution of 11.2 eV at 640 eV the line splitting between Mn L α and L β is visible. The ability to measure Mn fluorescence in the presence of large amounts of O is interesting for various biological studies, e.g. the study of photosystem II which is a protein containing Mn [26]. These measurements are very difficult with conventional detectors because of significant line overlap between O K and Mn L.

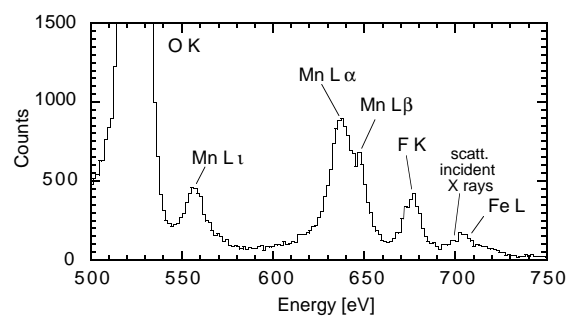


Fig. 14. Fluorescence spectrum of MnO sample with incident beam energy of 700 eV

In Fig. 15 we show the first X-ray fluorescence spectrum using an STJ detector to measure the L lines from a metalloprotein. Here we used a  $200 \times 200 \mu\text{m}^2$  detector with 50 nm-thick Al traps. The sample was ferredoxin, a protein containing iron. The incident energy was 780 eV with an energy width of about 20 eV. The resolution of the O K line was 11 eV FWHM.

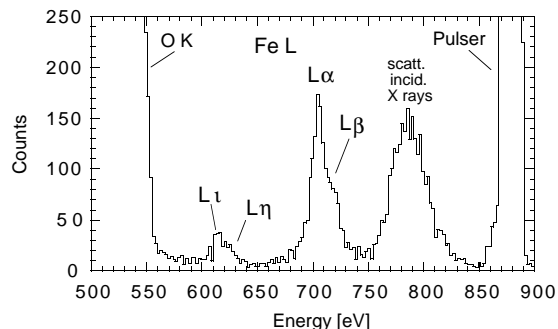


Fig. 15. Fluorescence spectrum of ferredoxin sample with incident beam energy of 780 eV.

## 6 Mass spectrometry

At LTD-6 Twerenbold [27] proposed using low-temperature detectors to measure the arrival of large biomolecules in a time-of-flight mass spectrometer (TOF-MS). The Human Genome Center Instrumentation Group at Lawrence Berkeley National Laboratory (LBNL) have been working for many years on improving the performance of TOF-MS systems. They had considered using "cryogenic bolometers" for TOF-MS back in 1991 [28] but at the time they only had access to thermal microcalorimeters which were too slow to be useful for this type of application. Our STJ detectors, however, are ideally suited for TOF-MS.

Working with LBNL group, we installed a small pumped-liquid helium cryostat with STJ detectors on their Matrix-Assisted Laser Desorption/ Ionization (MALDI) TOF-MS system [29]. We used a  $200 \times 200 \mu\text{m}^2$  Nb/Al<sub>2</sub>O<sub>3</sub>/Nb STJ detector with no Al trapping layers operating at 1.3 K. A pair of collimators cooled to 1.3 K, each with a 2 mm hole was placed in front of the STJ detector to limit its exposure to infrared radiation emitted from the flight tube at 300 K. The TOF MS was also equipped with a standard microchannel plate (MCP) detector to allow direct comparisons between STJ and MCP efficiencies [30].

A schematic of our dual-detector mass spectrometer is shown in Fig. 16. In our MALDI process, a nitrogen laser emitting 3 ns pulses of 335 nm light desorbs and ionizes molecular components embedded in a UV-sensitive matrix. The resulting ions are accelerated by a high voltage and propagate ballistically through the flight tube. Deflection plates in the flight tube afford the opportunity to aim ions either toward the STJ detector or a dual 25 mm diameter MCP mounted off axis. Measuring the ion flight time,  $\Delta t$ , through the evacuated flight tube from launch to arrival at the STJ detector or the MCP provides a way to calculate the ion mass,  $M$ . Neglecting the short time and distance for the initial acceleration,  $M = 2qU (\Delta t/L)^2$  where  $L$  is the length of the flight path of

a molecular ion of charge  $q$  accelerated by a voltage  $U$ . The rise times of the ion-induced tunneling current pulses were limited to  $\sim 500$  ns by the slow rise of the FET-based preamplifier. The onset of a pulse, i.e., the arrival time of an ion, could be determined with an accuracy better than 200 ns, which in principle, provides a mass resolution of 0.2 % at 66 kDa.

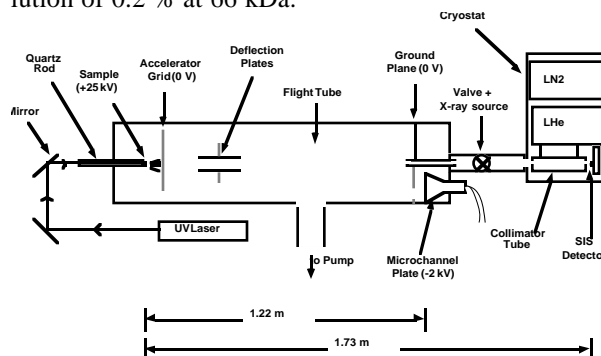


Fig. 16. The MALDI TOF-MS with MCP and STJ.

In Fig. 17 we show a time-of-flight spectrum of human serum albumin (HSA). The singly-charged and doubly-charged albumin peaks can easily be identified. The  $\sim 3 \mu\text{s}$  width of the albumin peaks is much larger than the time resolution of our detector and possibly is caused by straggling of the ion energy due to ion drag in the MALDI plume and electrical field inhomogeneity [31] or by fragmentation of the ions during acceleration [32].

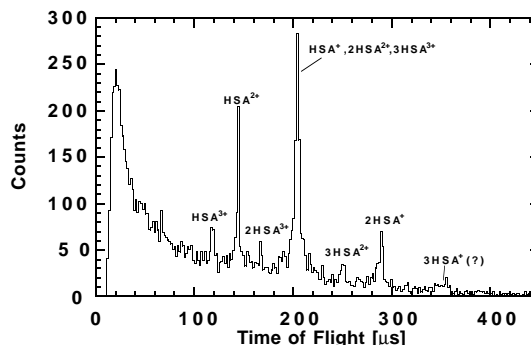


Fig. 17. The mass spectrum of human serum albumin measured with an STJ detector.

Our data indicate that the detection efficiency per unit area of the STJ detector for 25 keV albumin ions is about two to three orders of magnitude higher than that of the MCP. To estimate the number of events registered by each detector we co-added a large number of single shot spectra obtained with each detector and measured the total area of each  $\text{HSA}^+$  peak. The average pulse heights and decay times are known for each detector. Thus, for each detector the number of events in the  $\text{HSA}^+$  peak can be estimated from the peak area. After 500 single-shot spectra measured with the STJ detector were summed we estimated that the total number of ions in the singly

charged albumin peak was 1400. A similarly summed time-of-flight spectrum obtained with the MCP contained an estimated 11,700 pulses in the singly-charged albumin peak for 100 laser shots. Note that the active area of our STJ detector is 12,500 times smaller than that of the MCP. Normalizing the numbers of pulses to detector area we find a 300 times larger detection efficiency per unit area for the STJ detector. In deriving this number we neglected the effects of sample inhomogeneity, the 40% longer distance to the STJ detector which produces ion beam expansion and reduces the flux at the STJ detector, and a minor change of the ion beam profile when it is deflected towards the MCP. We estimate that these effects may cause an uncertainty in the derived detection efficiency by as much as a factor three, a small factor relative to the estimated 300-fold difference in sensitivity. Conservatively we conclude that at 66 kDa the STJ detector is between 2 and 3 orders of magnitude more sensitive per unit area than the MCP.

We have also demonstrated experimentally for the first time that the energy dependent response of the STJ detector provides a way to discriminate ions of different charge [33]. Doubly-charged ions, for example, carry twice the kinetic energy of singly-charged ions of equal mass and generate pulses with about twice the height. In Fig. 18 we show a scatter plot of pulse height versus flight time (for the same data as used for Fig. 17). Every point in this plot corresponds to a single ion striking the detector.

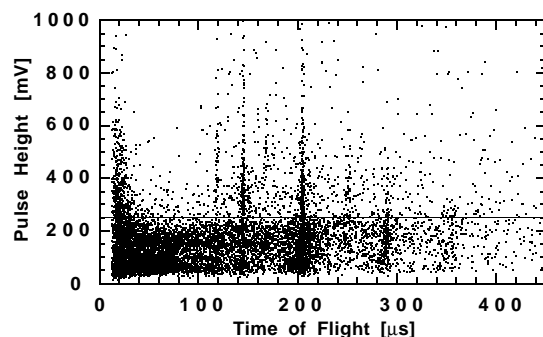


Fig. 18. Scatter plot of the STJ pulse height as a function of ion flight time.

The "dark band" of events with pulse heights smaller than about 250 mV can be assigned to singly charged ions. This can be seen if a pulse height cut is made at 250 mV along the indicated line in this figure. The time-of-flight spectrum for a collection of ions with pulse heights < 250 mV (Fig. 19) shows peaks that are assigned mostly to singly-charged ions. Peaks assigned to multiply-charged ions are removed or at least strongly suppressed in Fig. 19 by removing pulses larger than 250 mV. In contrast, the time-of-flight spectrum of events with pulse height > 250 mV (Fig. 20), contains mostly multiply-charged ions. These plots of energy-segregated pulses clearly demonstrate that an energy-resolving STJ detector helps to facilitate peak assignments.

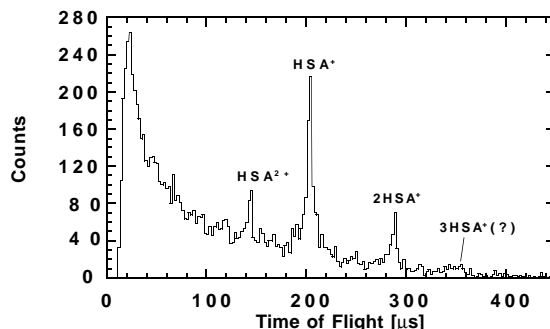


Fig. 19. The mass spectrum of HSA including only pulses less than 250 mV in height, selecting mostly singly charged ions.

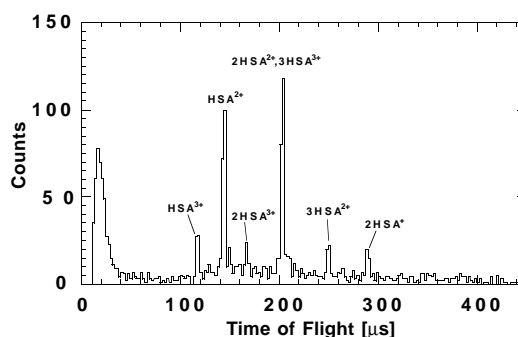


Fig. 20. The mass spectrum of HSA including only pulses more than 250 mV in height, selecting mostly multiply charged ions.

The pulse height cut at 250 mV does not discriminate perfectly singly-charged ions from multiply-charged ones as evidenced by the presence of the HSA<sup>2+</sup> ion peak in Fig. 19 and 2HSA<sup>+</sup> in Fig. 20. Imperfect discrimination occurs for two reasons. First, this STJ detector shows a poorer energy resolution for macromolecular ions than for X rays. The energy resolution of this STJ detector appears to be only 20 keV (FWHM) for macromolecules and therefore pulse height distributions from singly and doubly-charged ions overlap and cannot be perfectly separated. This rather poor resolution for macromolecules is in contrast to the observed FWHM resolution of 300 eV for 6 keV X rays. Second, the top of the dark band comprising singly-charged pulses (Fig. 18) is not flat and perhaps the height of the cut should increase with flight time.

There are several possible reasons for the poor energy resolution and rising pulse height with flight time. Fragmentation of the molecules during the acceleration might explain both effects [32]. We modeled this fragmentation and found that if the molecules break apart near the beginning of the acceleration, the energy of the fragments will vary with mass, resulting in a distribution of pulse heights rising with flight time. We also find that when fragmentation occurs near the final accelerating

grid, a large variation in measured energy will result. This will make the resolution for molecules appear very broad as observed.

We have also measured the much heavier protein macroglobulin, which is a tetramer with a total mass of 700 kDa. Initial measurements of macroglobulin showed a peak corresponding to a mass of 350 kDa, but very little of the full molecule appeared to survive the MALDI process. We then used chemical cross-linking to stabilize the full molecule. The spectrum of the cross-linked Macroglobulin is shown in Fig. 21. As can be seen in Fig 21, we have a significant detection of a 750 kDa molecule. No signal at this high a mass was detectable with the MCP detector. We also can see the effect of the cross-linking which has added an additional 50 kDa to the macroglobulin, presumably two units of a 25 kDa protein present in the original sample before cross-linking.

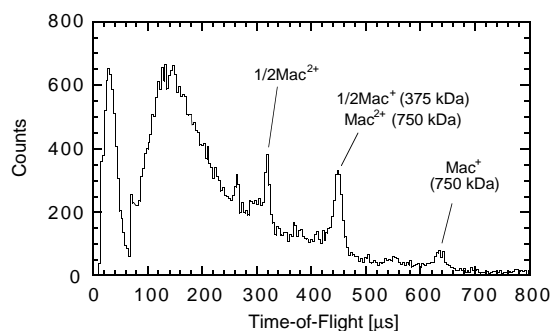


Fig. 21. The mass spectrum of macroglobulin after chemical cross linking.

We plan to continue studying how STJ detectors work in TOF-MS systems. We have found that the energy sensitivity of the STJ detector is an extremely useful tool both for separating different charge states, and for understanding and improving the launching mechanism. We are also beginning to use TOF-MS with STJ detectors to study molecule complexes like DNA repair proteins and understand how they operate.

## 7 Ta Crystal Detectors

We are also developing detectors based on ultra-pure single crystals of Ta. In such crystals the mean free path of the quasiparticles can be very long, allowing diffusion over distances much longer than possible with thin films.

We usually calculate this mean free path from the residual resistance ratio (RRR) which is the ratio of the resistance at room temperature to the resistance at a temperature low enough that the resistance is dominated by impurities and no longer varies with temperature. We have measured RRR values as high as 2000 for some of our ultra-pure Ta crystals [34]. By contrast, the best RRR values obtained for thin films grown epitaxially is

about 100 [35]. In principle, one can use superconducting crystals to scale up the absorber size considerably while maintaining the same diffusion time across the device. These crystal-based detectors therefore have the potential to provide high spectral resolution and high efficiency throughout the X-ray band and even into the lower-energy gamma-ray band, perhaps as high as 500 keV. These detectors can in principle be much larger than any of the current cryogenic X-ray detectors [20].

Photons absorbed in the Ta break up the Cooper pairs and create large number of quasiparticles and phonons. By attaching quasiparticle traps and thin-film sensors to the surface of the crystals we can measure both the quasiparticles and phonons and thus determine the energy of the absorbed photons. By measuring signals from different sensors at different locations on the crystal, we can unfold the position where the photon was absorbed [36, 37].

We are exploring the use of sensors based on superconductor insulator superconductor (SIS) tunnel junctions, superconductor insulator normal metal (SIN) tunnel junctions and superconducting transition-edge sensor (TES) for our crystal-based detectors. There are different fabrication issues for each sensor, as well as different operating characteristics. It is not yet clear which one will work best for this application. We therefore plan to test all three types in optimizing this detector.

To prepare the Ta crystals, we first cut slices of a few mm thick by EDM (spark erosion). We then polish the surface of the crystals mechanically, and then chemically etch the surface to remove damage from polishing and to further reduce the roughness. The etching solution is as follows: 25 ml HF (40%) : 25 ml HNO<sub>3</sub> (65%) : 25 ml H<sub>2</sub>SO<sub>4</sub> (96%) : 2 ml H<sub>2</sub>O [38]. We found that the surface roughness after the chemical polish depended very strongly on the exact composition of the etchant. The initial removal rate with this recipe is about 20 μm per minute, but quickly drops to a lower level. After eight minutes of etching, a total of 100 μm is removed from the surface. Typical samples have a roughness of 4.3 Å rms for a 10 × 10 μm<sup>2</sup> area. After the chemical polishing the surface is covered with a thin layer of photoresist and rectangular pieces are cut from the disks using an EDM. These samples are then cleaned and again chemically etched with the same etchant for 2-3 minutes to remove the crystal damage due to the EDM. In the future we will also re-anneal the crystals to remove interstitial gases that were introduced in processing. We have recently completed an ultra-high vacuum annealing furnace for this purpose.

We have tried several different approaches to fabricating Al/Al<sub>2</sub>O<sub>3</sub>/Al tunnel junctions on the surface of superconducting crystals [34, 39]. A schematic cross-section of our successful Al/Al<sub>2</sub>O<sub>3</sub>/Al tunnel junctions on the surface of a 2 × 6 × 12 mm<sup>3</sup> Ta crystal is shown in Fig. 22. All the metal films were deposited by dc magnetron

sputtering and structured using BeCu shadow masks. A 200 nm-thick Al base film was deposited and then oxidized for 30 minutes at 1.0 Torr, after which a 200 nm thick Al counter electrode was deposited. A 750 nm thick layer of SiO<sub>2</sub> is then deposited by rf magnetron sputtering with contact holes defined by means of lift-off. Al wiring layers are then deposited and the junctions are contacted by ultra-sonic wire bonding.

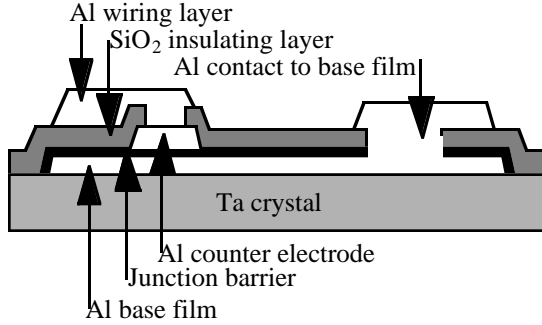


Fig. 22. SIS junction fabrication on Ta crystal.

The area of the junction is  $100 \times 100 \mu\text{m}^2$ , and the measured normal resistance  $R_N$  is  $1.21 \Omega$ . We use the ratio of  $R_D$ , the dynamic resistance in the sub gap region, to  $R_N$ , the normal state resistance of the tunnel junction, to parameterize the junction quality. This junction had a quality factor of  $2 \cdot 10^5$ , comparable to that of similar junctions fabricated on a Si substrate.

Due to the proximity effect of the Ta crystal on the 200 nm-thick Al base electrode, we measured a sum-gap voltage of  $440 \mu\text{eV}$ . From this we can see that the energy gap of the Al base electrode is raised to  $270 \mu\text{eV}$ , compared to the  $170 \mu\text{eV}$  for the Al counter electrode. We measured the I-V characteristics at different applied magnetic fields and found that the critical field of the Al base electrode was 20 mT, compared to 10 mT for the Al counter electrode. Thus, for applied magnetic fields between 10 mT and 20 mT the Al/Al<sub>2</sub>O<sub>3</sub>/Al junction on a Ta crystal behaves as an SIN tunnel junction with a superconducting base electrode and a normal counter electrode. To suppress the supercurrent a magnetic field of about 5 mT was needed.

For the fabrication of the TES devices we prepared the Ta crystals in the same way described above. The TES films were deposited by DC magnetron sputtering and structured by means of lift-off. They are  $0.5 \times 2.0 \text{ mm}^2$ , and positioned on the edges of the crystal. The thicknesses of the Cu and Al films are 35 and 55 nm respectively. The TES films have a normal resistance  $R_N$  of  $1.3 \Omega$  and a transition temperature of 90 mK. The transition width was less than 1 mK.

The structures described above demonstrate that we have successfully fabricated high-quality TES and SIS sensors on the surface of small Ta crystals. These structures, however, do not yet have all the proper trapping

layers to operate as actual detectors. Now that our fabrication techniques have been defined, we will begin fabricating more complete detectors with several different designs. Quasiparticles will be trapped by either an Al or normal-metal layer. For the largest devices, we intend to diffusion bond thin Al crystals to the Ta crystal. The quasiparticles would then be trapped further in a thin-film of normal metal. The resultant heating of the normal metal films would be measured TES or SIN sensor.

## 8 Transition-Edge Sensors

A TES is typically made of a thin film of low  $T_c$  superconductor which is operated in the transition between the superconducting and normal states. In the phase transition, resistance increases sharply with increasing temperature. This makes the TES a very sensitive thermometer that can be used to measure the hot electrons in a normal metal [40]. The sensitivity of the TES is usually described in terms of the parameter  $\alpha$ , which is the normalized resistance change for a temperature change at the operating point.

$$\alpha = \frac{T}{R} \frac{dR}{dT}. \quad (6)$$

In practice,  $\alpha$  is typically measured with very low currents where the resistance rises sharply with temperature. In operating a sensor, however, one typically biases the device with much more current, often enough to raise the temperature of the device significantly above the bath temperature.

We have developed a new model describing the TES. This model includes the current dependence of the TES resistance in addition to its temperature dependence [41, 42]. Based on our model, we derive new expressions for the theoretical limiting energy resolution of TES calorimeters and the pulse shape. We describe conditions under which the devices operate in a stable, unstable, or oscillatory fashion. Our theory is a generalization of bolometer theory, but the derivation is simpler than that presented by Jones [43], Mather [44] and Moseley *et al.* [45] because we proceed more directly by linearizing the differential equations, rather than using complex impedance formalism.

A TES is held at equilibrium on the transition by applying a dc voltage across it and by thermally grounding it to a cold bath so that Joule heating balances cooling into the bath. An illustration of the thermal and electrical circuits is shown in Fig. 23. Under a voltage bias, the electrical current through the device decreases with increasing resistance. Therefore, heating of the device drives the current down. The decrease in current is measured with a sensitive dc SQUID ammeter, and the pulse heights are approximately proportional to the energy in the events. Excellent performance has been demonstrated

with an X-ray microcalorimeter based on a TES coupled to a normal metal film [19].

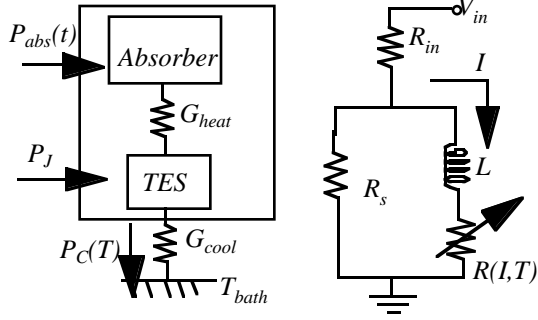


Fig 23. The thermal (left) and electrical (right) circuit.

The TES is typically connected to a bias circuit as illustrated in Fig. 23. If the resistance of the shunt resistor,  $R_s$ , is chosen to be small compared to resistance of the TES,  $R(I, T)$ , the circuit biases the TES with a voltage bias (at zero frequency)  $V = V_{in}(R_s / R_{in} + R_s)$  where  $V_{in}$  is the input voltage applied to the circuit,  $R_{in}$  is a large resistor in series with the voltage source. This part of the circuit functions as a voltage divider, reducing the applied voltage to a voltage suitable to bias the TES. If  $R_s \gg R(I, T)$  the TES is current biased.

In practice, the inductance of the circuit,  $L$ , is dominated by the inductance coil of the dc SQUID array current amplifier, which is in series with the TES. The SQUID measures the current,  $I$ , through the TES. The electrical circuit is described by the following equation:

$$L \frac{dI}{dT} = \frac{V_{in} R_s}{R_{in} + R_s} - I \left( \frac{R_{in} R_s}{R_{in} + R_s} + R(I, T) \right). \quad (7)$$

We have assumed that the wires connecting the SQUID to the TES are superconducting. For simplicity, we have neglected parasitic resistances.

The thermal circuit is also illustrated in Fig. 23. The TES is thermally connected to an absorber and to a cold bath at a temperature,  $T_{bath}$ . In this model, we assume that the TES and absorber can be regarded as having a common temperature,  $T$ , and heat capacity,  $C(T)$ . This is true if the TES and absorber thermally equilibrate on a time scale that is fast compared to the cooling time of the TES, and fast compared to the characteristic time constant of the electrical circuit,  $\tau_{el}$  (defined in Eq. 10). In this case, the TES and absorber can be regarded as equilibrating instantaneously.

In this model, the thermal circuit is described by the following equation:

$$C(T) \frac{dT}{dt} = P_J(I, T) - P_c(T) + P_{abs}(t) \quad (8)$$

where  $P_J(I, T) = I^2 R(I, T)$  is the Joule Heating due to the voltage bias. And,  $P_c(T)$  is the power of the cooling into the cold bath.  $P_{abs}(t)$  is the input power caused by an event depositing an energy  $E$ , at time  $t = t'$ , giving a power  $P_{abs}(t) = E \delta(t - t')$ .

The cooling of the TES is typically limited by the electron-phonon coupling, which is described by a power law:  $P_c(T) = \Sigma \Omega_{TES} (T^N - T_{bath}^N)$  where  $\Omega_{TES}$  is the volume of the film where electron-phonon interaction is dominant. The constants  $\Sigma$  and  $N$  are material dependent parameters; for a normal metal like silver,  $N=5$  in the 50 to 100 millikelvin range [46].

In order to derive simple analytical expressions for pulse shape, noise, and energy resolution, it is necessary to simplify the differential equations that describe the TES microcalorimeter. Near equilibrium,  $(I_0, T_0)$ , Eqs. 7 and 8 can be approximated by coupled linear partial differential equations:

$$\frac{d}{dt} \begin{pmatrix} \delta I \\ \delta T \end{pmatrix} = \begin{pmatrix} \tau_{el}^{-1} & -A \\ B & \tau_{th}^{-1} \end{pmatrix} \begin{pmatrix} \delta I \\ \delta T \end{pmatrix} \quad (9)$$

where  $\delta I = I - I_0$ , and  $\delta T = T - T_0$ . The linearized equations are obtained by taking the Taylor expansion of the Eqs. 7 and 8 about the equilibrium point, and then neglecting terms with order higher than first order. The matrix contains a number of constants, which represent coefficients in the Taylor expansion. We now define these coefficients and describe their physical meaning.

The electric time constant,  $\tau_{el}$ , gives the response time of the electrical circuit, which is limited by the inductance  $L$ . It measures how quickly the electric circuit can respond to changes in the TES.

$$\tau_{el}^{-1} = \frac{1}{L} \left( \frac{R_{in} R_s}{R_{in} + R_s} + R_0 + I_0 \left[ \frac{\partial R(I, T)}{\partial I} \right]_0 \right) \quad (10)$$

The thermal time constant,  $\tau_{th}$ , gives the time scale of thermal changes in the TES.

$$\tau_{th}^{-1} = \tau_J^{-1} - \tau_{cool}^{-1} \quad (11)$$

The thermal time constant in turn depends on two other time constants. The cooling time constant,  $\tau_{cool}$ , represents the characteristic time scale of the cooling into the cold bath.

$$\tau_{cool}^{-1} = \left[ \frac{\partial}{\partial T} \left( \frac{P_c(T)}{C(T)} \right) \right]_0 \quad (12)$$

The Joule heating time constant,  $\tau_J$ , measures the time scale of changes in the Joule heating due to temperature perturbations.

$$\tau_J^{-1} = I_0^2 \left[ \frac{\partial}{\partial T} \left( \frac{R(I, T)}{C(T)} \right) \right]_0 \approx \tau_{cool}^{-1} \frac{\alpha'}{N} \left( 1 - \frac{T_{bath}^N}{T_0^N} \right) \quad (13)$$

where the approximation holds in the case when  $C(T)$  is constant, and  $\alpha'$  is the steepness of the transition at the operating point.

$$\alpha' = \frac{T_0}{R_0} \left[ \frac{\partial R(I, T)}{\partial T} \right]_0 \quad (14)$$

Note that  $\alpha'$  in Eq. 14 is not the same as commonly used  $\alpha$  in Eq. 6. The constant  $\alpha'$  is the partial derivative of the TES resistance with respect to temperature and evaluate at the operating current  $I_0$ . Typically  $\alpha'$  will be smaller than  $\alpha$ .

The thermal time constant may be either positive or negative, depending on whether or not Joule heating effects dominate over the cooling. If  $\alpha'$  is much larger than one, then the Joule heating time usually dominates.

The cross terms in Eq. 9 are defined as follows:

$$A = \frac{I_0}{L} \left[ \frac{\partial R(I, T)}{\partial T} \right]_0 = \frac{I_0}{L} \frac{R_0}{T_0} \alpha' \quad (15)$$

$$B = \frac{1}{C(T_0)} \left[ \frac{\partial P_J(I, T)}{\partial I} \right]_0 \quad (16)$$

The product of the cross terms describe the strength of the coupling between the electrical and thermal parts of the system. So we define the electro-thermal feedback time constant  $\tau_{eff}^{-2} = AB$ .

The coupled equations in Eq. 9 can be solved by standard methods. The solution can then be used to describe the reaction of the system to a sudden temperature rise  $\Delta T = E/C(T)$ . The eigenvalues of the matrix in Eq. 9 give the negative reciprocal of the rise time and decay time of the measured current pulse. The eigenvectors indicate the path of the recovery in the  $I, T$  plane, as is shown in Fig. 24. The eigenvalues must both be negative for the device to operate in a stable fashion. If  $\tau_{th} > 0$ , i.e.  $\tau_{cool} > \tau_J$ , this results in the following constraints:

$$\tau_{th} > \tau_{el} \quad (17)$$

$$\tau_{th} \tau_{el} > \tau_{eff}. \quad (18)$$

And to avoid oscillations, the eigenvalues must be real requiring:

$$(\tau_{th}^{-1} + \tau_{el}^{-1})^2 > 4\tau_{eff}^{-2} \quad (19)$$

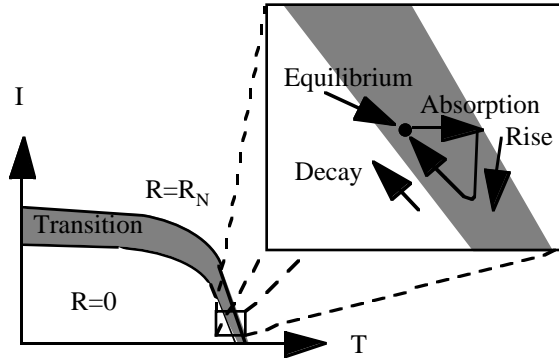


Fig. 24. The response of the TES to an energetic event.

To add noise to this linear model, we add terms to the differential equations to account for voltage fluctuations due to Johnson noise and thermal fluctuations due to phonon noise. The linearized equations for small perturbations from equilibrium are

$$\frac{d}{dt} \begin{pmatrix} \delta I \\ \delta T \end{pmatrix} = \begin{pmatrix} \tau_{el}^{-1} & -A \\ B & \tau_{th}^{-1} \end{pmatrix} \begin{pmatrix} \delta I \\ \delta T \end{pmatrix} + \begin{pmatrix} \dot{I}_{JN}(t) \\ \dot{T}_{PN}(t) \end{pmatrix} \quad (20)$$

where  $\dot{I}_{JN}(t) = V_{JN}(t)/L$  is the Johnson noise term and  $\dot{T}_{PN}(t) = P_{PN}(t)/C(T)$  is the phonon noise term. We then take the Fourier transform and solve for  $|\delta I_\omega|^2$  and  $|\delta T_\omega|^2$ , the power spectra of the current and temperature

fluctuations. Note that the Johnson noise and the phonon noise are not correlated to each other, so they add in quadrature.

$$\begin{pmatrix} |\delta I_\omega|^2 \\ |\delta T_\omega|^2 \end{pmatrix} = D(\omega)^2 \begin{pmatrix} \omega^2 + \tau_{th}^{-2} & A^2 \\ B^2 & \omega^2 + \tau_{el}^{-2} \end{pmatrix} \begin{pmatrix} |\dot{I}_{JN}(\omega)|^2 \\ |\dot{T}_{PN}(\omega)|^2 \end{pmatrix} \quad (21)$$

where

$$D(\omega)^{-1} = \det \begin{pmatrix} i\omega + \tau_{th}^{-1} & A \\ B & i\omega + \tau_{el}^{-1} \end{pmatrix} \quad (22)$$

and the power spectra of the Johnson and thermal noise are  $|\dot{I}_{JN}(\omega)|^2 = 4k_B T_0 R_0 / L$  and  $|\dot{T}_{PN}(\omega)|^2 = 2k_B (T_0^2 + T_{bath}^2) G(T) / C(T)$ .

We can now give the noise equivalent power per frequency,

$$|\text{NEP}(\omega)|^2 = \frac{C(T)^2 |\delta I_\omega|^2}{A^2 |D(\omega)|^2} \quad (23)$$

In the ideal case, the Johnson noise and the phonon noise dominate over other forms of noise due the experimental set up:  $|\text{NEP}(\omega)|^2 = |\text{NEP}_{JN}(\omega)|^2 + |\text{NEP}_{PN}(\omega)|^2$ . The energy resolution of device, when optimally filtered, is given by an integral of the noise equivalent power [[47]]. This yields

$$\Delta E_{FWHM} = 2.35 \sqrt{\tau_{th} |\text{NEP}_{JN}(0)| |\text{NEP}_{PN}(0)|} \quad (24)$$

In the case that the Johnson noise is much less than the phonon noise at zero frequency, which is expected for large  $\alpha'$ , the theoretical limiting energy resolution of the device is

$$\Delta E_{FWHM} \approx 2.35 \sqrt{\frac{4k_B T_0^2 C(T)}{\alpha'}} \sqrt{\frac{N}{2}} \sqrt{\left(1 + \frac{T_{bath}^2}{T_0^2}\right)} \quad (25)$$

The limiting energy resolution in Eq. 25 is similar in form to the expression derived previously by Irwin [48]. There are, however, several differences. The most important difference is that  $\alpha'$  (Eq 14) appears here rather than  $\alpha$  (Eq. 6). As described above,  $\alpha'$  is evaluated at the operating current with the current held fixed, and is typically smaller than  $\alpha$  measured at very low currents. In practice measuring  $\alpha'$  is not easy it requires a second sensitive thermometer coupled strongly to the TES. The result in Eq. 25 holds over a large range in bias conditions as the stability conditions in Eqs. 17, 18 and 19 are met. For large values of  $\alpha'$ , this will generally require  $R_S < R(I, T)$ . A more complete description of this model, including the full dynamical solution and the effects of amplifier noise is in preparation [49].

## Acknowledgments

We would like to thank Henry Benner, David Horn, Feng Zhong and Joe Jaklevic at LBNL for their assistance with the mass spectrometer measurements. We also wish to thank Jan Batteux, Dennis Carr, Steve Cramer, Jeff

Moore and Curtis Troxel for advice and expert technical support.

This work was performed under the auspices of the U.S. Department of Energy by Lawrence Livermore National Laboratory under contract no. W-7405-ENG-48. Some experiments were performed at the Stanford Synchrotron Radiation Laboratory (SSRL) which is operated by the Department of Energy, Office of Basic Energy Sciences under contract number is DE-AC03-76SF00515. This work was also supported by NASA SBIR contract NAS5-32805, NASA UV detector development grant NAGW 3907 and NASA Innovative Research Program contract W-18,868. JBIG acknowledges additional support from the Dutch Scientific Organization NWO.

## References

- [1] A.T. Barfknecht, *et al.*, IEEE Trans. Mag. MAG-27 (1991) 970.
- [2] M. Frank, *et al.*, NIM A 370 (1996) 41.
- [3] C.A. Mears, *et al.*, NIM A370 (1996) 53.
- [4] C.A. Mears, *et al.*, IEEE Trans. Appl. Supercon. 7 (1997) 3415.
- [5] S.E. Labov, *et al.*, IEEE Trans. Appl. Supercon. 5 (1995) 3034.
- [6] L.J. Hiller, *et al.*, SPIE Proc. 2518 (1995) 249.
- [7] N.E. Booth, Appl. Ph. L. 50 (1987) 293.
- [8] P.T. Timbie, *et al.*, Cryogenics 30 (1990) 271.
- [9] S. Labov, *et al.*, in *Low Temperature Detectors for Neutrinos and Dark Matter IV*, N.E. Booth and G.L. Salmon, Ed. 1992, p. 285.
- [10] C.A. Mears, *et al.*, J. X-ray Sci. Tech. (1997) in press.
- [11] J.B.I. Grand, *et al.*, Physica C 279 (1997) 85.
- [12] C.A. Mears, *et al.*, Appl. Ph. L. 63 (1993) 2961.
- [13] D.J. Goldie, *et al.*, Appl. Ph. L. 64 (1994) 3169.
- [14] M. Kurakado, NIM 196 (1982) 275.
- [15] N. Rando, *et al.*, NIM 313 (1992) 173.
- [16] J.B.I. Grand, *et al.*, (1997) in preparation.
- [17] D. McCammon, *et al.*, NIM A326 (1993) 157.
- [18] E. Silver, *et al.*, X-Ray Spec. 25 (1996) 115.
- [19] D.A. Wollman, *et al.*, J. Microscopy (1997) submitted.
- [20] S.E. Labov, *et al.*, NIM A370 (1996) 65.
- [21] M. Frank, *et al.*, Rev. Sci. Inst. (1997) submitted.
- [22] C.A. Mears, *et al.*, IEEE Trans. Appl. Supercon. 5 (1995) 3069.
- [23] A. Poelaert, *et al.*, Proceedings SPIE 2808 (1996) 523.
- [24] J.B.I. Grand, *et al.*, (1997) in preparation.
- [25] M. Mantler, Prog. Crystal Growth and Charact. 14 (1987)
- [26] S.P. Cramer, *et al.*, NIM A319 (1992) 285.
- [27] D. Twerenbold, NIM A370 (1996) 253.
- [28] J.M. Jaklevic, *et al.*, *Advanced Detectors for Mass Spectrometry* 1991, Lawrence Berkeley National Laboratory:
- [29] W.H. Benner, *et al.*, Rap. Comm. Mass Spec. 9 (1995) 537.
- [30] M. Frank, *et al.*, Rap. Comm. Mass Spec. 10 (1996) 1946.
- [31] J. Zhou, *et al.*, Rap. Comm. Mass Spec. 6 (1992) 671.
- [32] M. Frank, *et al.*, (1997) in preparation.
- [33] W.H. Benner, *et al.*, J. Am. Mass Spec. Soc. (1997) submitted.
- [34] H. Netel, *et al.*, NIM A370 (1996) 47.
- [35] H. Kraus, *et al.*, J. Low T. Ph. 93 (1993) 533.
- [36] H. Kraus, *et al.*, Phys. Rev. B 231 (1989) 195.
- [37] S. Friedrich, *et al.*, IEEE Trans. Appl. Supercon. 7 (1997) 3383.
- [38] M.P. Bruijn, *et al.*, IEEE Trans. Appl. Supercon. 7 (1997) 3387.
- [39] H. Netel, *et al.*, SPIE Proc. 2518 (1995) 244.
- [40] K.D. Irwin, *et al.*, Appl. Ph. L. 69 (1996) 1945.
- [41] K.D. Irwin, Appl. Ph. L. 66 (1995) 1998.
- [42] K.D. Irwin, *et al.*, NIM A370 (1996) 177.
- [43] R.C. Jones, Opt. Soc. Am. 43 (1953) 1.
- [44] J.C. Mather, Applied Optics 21 (1982) 1125.
- [45] S.H. Moseley, *et al.*, J. Appl. Phys. 56 (1984) 1257.
- [46] F.C. Wellstood, *et al.*, Phys. Rev. B 49 (1994) 5952.
- [47] A.E. Szymkowiak, *et al.*, J. Low T. Ph. 93 (1993) 281.
- [48] K.D. Irwin, Ph.D. Thesis (1995) Stanford University.
- [49] M.A. Lindeman, *et al.*, (1997) in preparation.